

## Low-Resolution Optical Spectroscopy

Our first spectra of SN 2011fe were obtained with the FRODOSpec instrument on the Liverpool Telescope (La Palma, Canary Islands, Spain). This dual-beam integral-field unit (IFU) spectrograph gives a resolving power of 2200. The supernova (SN) was observed on August 24, starting at 20.7 (UT dates are used throughout) with an exposure time of 1800 s. The wavelength coverage is 3900–5600 Å in the blue arm and 5900–9000 Å in the red arm. The raw spectra for each fiber of the IFU were extracted using a custom-built pipeline. This resulted in a sky-subtracted and wavelength-calibrated spectrum for each fiber. They were then combined together and a flux calibration was applied.

We also obtained low-resolution optical spectra of SN 2011fe with the Kast spectrograph<sup>28</sup> mounted on the 3 m Shane telescope at Lick Observatory beginning at 04:05 on 2011 August 25. It was taken with a 2'' wide slit, and a 600/3410 grism on the blue side and a 300/7500 grating on the red side, resulting in full width at half-maximum (FWHM) resolutions of  $\sim 4$  and 6 Å, respectively. The spectrum was aligned along the parallactic angle to reduce differential light losses<sup>29</sup>. All spectra were reduced using standard techniques. Routine CCD processing and spectrum extraction were completed with IRAF, and the data were extracted with an optimal algorithm<sup>30</sup>. We obtained the wavelength scale from low-order polynomial fits to calibration-lamp spectra. Small wavelength shifts were then applied to the data after cross-correlating a template sky to the night-sky lines that were extracted with the SN. We fit spectrophotometric standard-star spectra to the data in order to flux calibrate our spectra and to remove telluric lines<sup>31,32</sup>.

The results of these observations are plotted in Figure 2 of the main text.

## High-Resolution Optical Spectroscopy

We observed SN 2011fe with the High Resolution Echelle Spectrometer (HIRES<sup>33</sup>) mounted on the 10 m Keck I telescope beginning at 5:51 on 2011 August 25 (only 1.6 day after our derived explosion date). The spectrum was reduced using standard techniques, and normalised by fitting the continuum in each echelle order with low-order polynomials. Wavelength calibration was performed relative to a series of emission-line lamps, and then corrected to the Solar System barycenter frame of reference. A cutout of the resulting normalised spectrum, centred on the rest-frame Na I  $\lambda\lambda$ 5890, 5896 doublet, is shown in Figure 2 of the main text.

In this wavelength range, we identify only a single significant absorption feature. Fitting a Gaussian profile to this line, we measure a central wavelength of  $\lambda = 5893.75 \pm 0.02$  Å and a FWHM of  $0.184 \pm 0.009$  Å. The inferred line equivalent width is  $W = 0.045 \pm 0.009$  Å.

If we associate this feature with Na I  $\lambda$ 5890 (the stronger of the two components in the doublet), the observed wavelength is offset from the rest wavelength by  $\Delta v = +194$  km s<sup>-1</sup>. Similarly, the line is blueshifted from the systemic velocity of M101 ( $v = 241 \pm 2$  km s<sup>-1</sup>)<sup>34</sup> by  $\Delta v = -47$  km s<sup>-1</sup>. Given the high Galactic latitude ( $b = 59.8^\circ$ ), we consider it likely that the absorbing material originates in M101.

Independent of the origin of the absorbing material, the lack of strong Na I features indicates that the line of sight to SN 2011fe is affected by a negligible amount of extinction. Using common scaling relations<sup>35</sup>, the observed equivalent width corresponds to an optical extinction of  $A_V = 0.04$  mag.

## Swift UltraViolet/Optical Observations

Immediately upon discovery we triggered target-of-opportunity observations of SN 2011fe with the *Swift* satellite<sup>36</sup>. Observations with the UltraViolet-Optical Telescope (UVOT<sup>37</sup>) began at 22:08 on 24 August 2011. We retrieved the level 2 UVOT data for SN 2011fe from the *Swift* data archive. To increase the signal-to-noise ratio, we stacked the images for each individual filter on a daily basis. To remove host-galaxy contamination underlying the SN location, we subtracted pre-outburst images of M101 obtained by the UVOT. We caution that, due to the nonlinearity of the coincidence-loss correction, such a technique can lead to modest systematic uncertainties in the SN flux, particularly

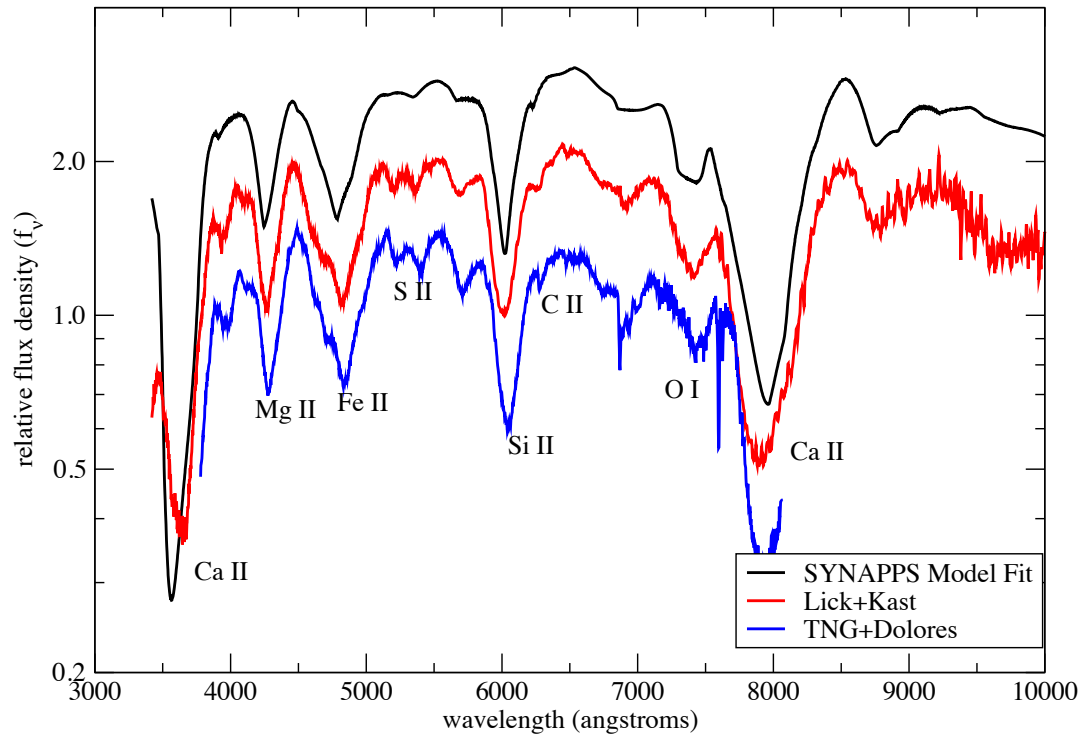
MJD	Telescope/Instrument	Filter	Exp. Time (s)	Magnitude
55795.199	P48	<i>g</i>	120.0	> 21.5
55797.166	P48	<i>g</i>	60.0	17.349 ± 0.011
55797.209	P48	<i>g</i>	60.0	17.155 ± 0.011
55797.923	<i>Swift</i> /UVOT	<i>uvw1</i>	314.49	18.90 ± 0.21
55797.925	<i>Swift</i> /UVOT	<i>u</i>	157.04	16.68 ± 0.05
55797.926	<i>Swift</i> /UVOT	<i>b</i>	157.02	15.42 ± 0.09
55797.927	<i>Swift</i> /UVOT	<i>uvw2</i>	629.48	20.96 ± 0.39
55797.930	<i>Swift</i> /UVOT	<i>v</i>	157.02	15.12 ± 0.09
55797.931	<i>Swift</i> /UVOT	<i>uvm2</i>	3264.03	> 21.0
55798.156	P48	<i>g</i>	60.0	14.886 ± 0.010
55798.199	P48	<i>g</i>	60.0	14.839 ± 0.009
55799.001	<i>Swift</i> /UVOT	<i>uvw1</i>	618.60	17.35 ± 0.08
55799.002	<i>Swift</i> /UVOT	<i>u</i>	206.69	15.11 ± 0.03
55799.003	<i>Swift</i> /UVOT	<i>b</i>	206.63	13.86 ± 0.06
55799.003	<i>Swift</i> /UVOT	<i>uvw2</i>	1037.48	19.02 ± 0.26
55799.006	<i>Swift</i> /UVOT	<i>v</i>	276.45	13.62 ± 0.06
55799.006	<i>Swift</i> /UVOT	<i>uvm2</i>	1387.15	20.04 ± 0.29
55799.142	P48	<i>g</i>	30.0	13.787 ± 0.011
55799.164	P48	<i>g</i>	30.0	13.751 ± 0.013
55799.181	P48	<i>g</i>	30.0	13.713 ± 0.011
55799.202	P48	<i>g</i>	30.0	13.726 ± 0.013
55799.221	P48	<i>g</i>	30.0	13.701 ± 0.013
55799.239	P48	<i>g</i>	30.0	13.689 ± 0.012
55800.203	P48	<i>g</i>	30.0	12.964 ± 0.013
55800.221	P48	<i>g</i>	30.0	12.959 ± 0.012

**Supplementary Table 1** — UV/Optical Observations of SN 2011fe. P48 observations have been calibrated with respect to Sloan Digital Sky Survey *g*-band images of the field, and are on the PTF photometric system. *Swift*/UVOT images have been calibrated using standard recipes<sup>39</sup> and are reported on the AB system<sup>40</sup>.

at high count rates<sup>38</sup>. The photometric calibration was performed following standard recipes<sup>39</sup>, and the reported magnitudes are on the AB system<sup>40</sup>. The resulting photometry is presented in Supplementary Table 1.

## SYNAPPS Spectral Fits

We analysed the spectrum of SN 2011fe using the automated SN spectrum interpretation code SYNAPPS<sup>41</sup>. SYNAPPS uses a parallelised pattern search algorithm to compare highly parametrised synthetic spectra to observed ones to find a good fit. Results from SYNAPPS are useful for (a) identifying or rejecting the presence of ion signatures and (b) estimating characteristic ejecta velocities. Typical premaximum SN Ia ions are confirmed: O I, Mg II, Si II, S II, Ca II, and Fe II (Supplementary Figure 1). Fe III was not needed in the fit. In addition, the fit confirms the presence of C II  $\lambda\lambda$ 6580, 7234, though the detailed fit is not perfect, probably due to parametrisation bias. Both high-velocity (HV) Si II and Ca II are confirmed by SYNAPPS (extending above 21,000 km/s). Surprisingly, SYNAPPS finds HV O I (in excess of 20,000 km/s) for the absorption centered at 7400 Å. This is the first identification of variable high-velocity oxygen in the ejecta of a SN Ia in the literature to date. Furthermore we note that the change in velocity of the Mg II and Fe II features are ~4% and that of Si II is ~8% over the first 24 hr.



**Supplementary Figure 1** — A SYNAPPS fit to the Lick/Kast spectrum and the TNG/Dolores spectrum taken 16 hrs later. The agreement is excellent and we have confidently identified several intermediate-mass elements including high-velocity Ca II, Si II, and O I, the last of which forms the feature centered at 7400 Å.

## Parabolic Shape of the $^{56}\text{Ni}$ Powered Light Curve at Early Times

The  $L \propto t^2$  behaviour found for the early-time light curve of SN 2011fe is consistent with a simple fireball model in which the effective temperature remains fixed while the radius increases with time as  $r = v_p t$ . In reality, one expects the effective temperature to change with time, while the photospheric velocity  $v_p$  will decrease as the remnant expands and the density drops. However, the same  $t^2$  law can be derived by a more rigorous analytic argument that includes the effects of radiative diffusion,  $^{56}\text{Ni}$  energy deposition, and expansion losses<sup>42</sup>. We describe here a simple one-spatial-zone model for the whole remnant which shows that the observed rise,  $L \propto t^2$  at early times, is consistent with a  $^{56}\text{Ni}$  powered SN, with no contribution to the luminosity from the explosion shock wave or from interaction with circumstellar material or a companion star.

For the expanding remnant, the evolution of the internal energy,  $E_{\text{int}}$ , is given by the first law of thermodynamics,

$$\frac{\partial E_{\text{int}}}{\partial t} = -P \frac{\partial V}{\partial t} + L_{\text{Ni}}(t) - L_{\text{c}}(t), \quad (1)$$

where  $L_{\text{Ni}}$  is the energy deposited per second from  $^{56}\text{Ni}$  decay and  $L_{\text{c}}$  is the radiated luminosity. We assume that the  $^{56}\text{Ni}$  energy is thermalised throughout the remnant, and that radiation pressure dominates,  $P = E_{\text{int}}/3V$ . Assuming homologous expansion, the volume increases as  $V \propto t^3$  and equation 1 becomes

$$\frac{1}{t} \frac{\partial}{\partial t} [E_{\text{int}} t] = L_{\text{Ni}}(t) - L_{\text{c}}(t). \quad (2)$$

The radiated luminosity,  $L_{\text{c}}$ , is approximated from the diffusion equation

$$\frac{L_{\text{c}}}{4\pi R^2} = \frac{c}{3\kappa\rho} \frac{\partial E_{\text{int}}/V}{\partial r} \approx \frac{c}{3\kappa\rho} \frac{E_{\text{int}}/V}{R}. \quad (3)$$

In homologous expansion,  $R = v_{\text{f}} t$ , and the radiated luminosity can be rewritten

$$L_{\text{c}} = \frac{E_{\text{int}} t}{t_{\text{d}}^2}, \quad \text{where } t_{\text{d}} = \left[ \frac{3}{4\pi} \frac{M_{\text{ej}} \kappa}{v_{\text{f}} c} \right]^{1/2}. \quad (4)$$

Here, we defined the effective diffusion time  $t_{\text{d}}$ , and  $v_{\text{f}} = [E_{\text{sn}}/2M_{\text{ej}}]^{1/2}$  is the final characteristic ejecta velocity. For the case where the elapsed time is much less than the  $^{56}\text{Ni}$  decay time of  $\tau_{\text{Ni}} = 8.8$  day, the energy deposition from  $^{56}\text{Ni}$  decay can be considered constant with time ( $L_{\text{Ni}} = E_{\text{Ni}}/\tau_{\text{Ni}}$ ) and the solution of equation 4 is

$$L_{\text{c}}(t) \approx \frac{E_{\text{Ni}}}{\tau_{\text{Ni}}} [1 - e^{-t^2/2t_{\text{d}}^2}] \quad t \ll \tau_{\text{Ni}}, \quad (5)$$

where we have assumed that the initial internal energy of the ejecta (from the explosion shock) is negligible compared to the heating from  $^{56}\text{Ni}$  decay. For typical parameters, the effective diffusion time is  $\sim 20$  day, so taking the limit  $t \ll t_{\text{d}}$  gives

$$L_{\text{c}}(t) \approx \frac{E_{\text{Ni}}}{\tau_{\text{Ni}}} \frac{t^2}{2t_{\text{d}}^2} \quad t \ll t_{\text{d}}, t \ll \tau_{\text{Ni}}. \quad (6)$$

The validity of the argument can be questioned at these very early times, as the analysis does not properly capture the early transient phase in which a diffusion wave moves from the inner  $^{56}\text{Ni}$  core to the surface. However, the excellent fit of the observed light curve to a  $t^2$  law suggests that the simple model is not unreasonable. From the day 0.45 observation of SN 2011fe (luminosity  $L \approx 10^{40}$  erg  $\text{s}^{-1}$ ) and equation 6, we find a total  $^{56}\text{Ni}$  mass of  $0.45 M_{\odot}$ , comparable to the value inferred for a (slightly underluminous) normal SN Ia. This suggests that the early-time luminosity of SN 2011fe is consistent with  $^{56}\text{Ni}$  powering only, with little or no contribution from shocks.

## Contribution to the Early Luminosity from Shock Heating

At early times ( $\sim 1$  day), the diffusion of radiation from the ejecta shock-heated in the explosion may contribute to the emergent luminosity (in addition to the luminosity generated by  $^{56}\text{Ni}$  heating). Observations of this shock

luminosity can be used to constrain the radius of the progenitor star. Relevant models have been considered by many authors<sup>43,44,45,46,47,48,49</sup>, all of whom take a similar analytical approach to calculating the evolution of a radiation dominated, homologously expanding, constant opacity, spherically symmetric supernova remnant. The models differ in their assumptions of the initial ejecta density and pressure profiles and in the treatment of radiative diffusion. However, the final predictions of the early-time light curve tend to be quite similar.

Recent work has shown<sup>49</sup>, for the case of early cooling luminosity after shock breakout in a SN Ia, the luminosity and effective temperature follow:

$$\begin{aligned} L(t) &= 1.2 \times R_{10} 10^{40} E_{51}^{0.85} M_c^{-0.69} \kappa_{0.2}^{-0.85} f_p^{-0.16} t_d^{-0.31} \text{ erg s}^{-1}, \\ T(t) &= 4015 R_{10}^{1/4} E_{51}^{0.016} M_c^{0.03} \kappa_{0.2}^{0.27} f_p^{-0.022} t_d^{-0.47} \text{ K}, \end{aligned} \quad (7)$$

where  $E_{51}$  is the explosion energy  $E/10^{51}$  erg,  $R_{10}$  is the progenitor radius  $R/10^{10}$  cm,  $M_c$  is the total ejecta mass in units of the Chandrasekhar mass,  $\kappa_{0.2}$  is the opacity  $\kappa/0.2 \text{ cm}^2 \text{ g}^{-1}$ ,  $f_p$  is a dimensionless form factor, and  $t_d$  is the time since explosion in days. These results are similar to those found by earlier work<sup>45</sup> for ejecta in spherical expansion.

For the case of SN ejecta impacting a companion star in Roche-lobe overflow, self-similar diffusion arguments have shown that the post interaction luminosity is described by<sup>46</sup>:

$$\begin{aligned} L(t) &= 1.0 \times 10^{40} a_{10} E_{51}^{0.875} M_c^{-0.375} \kappa_{0.2}^{-0.75} t_d^{-0.5} \text{ erg s}^{-1}, \\ T(t) &= 4446 a_{10}^{1/4} E_{51}^{0.0} M_c^{0.0} \kappa_{0.2}^{0.97} t_d^{-0.51} \text{ K}, \end{aligned} \quad (8)$$

where  $a_{10}$  is the separation distance between the WD and its companion star in units of  $10^{10}$  cm. The isotropic equivalent luminosity here applies to a viewing angle aligned with the symmetry axis, and will be lower for off-axis viewing angles. Despite the somewhat different context and approach, the formulae are very similar to the previously discussed colling of the shock heated SN<sup>49</sup>, both in the scalings and the overall normalization. In particular, the luminosity depends linearly on  $R$  or  $a$ , while the effective temperature is proportional to  $R^{1/4}$  or  $a^{1/4}$ .

We used equations 7 and 8 to construct model spectra for progenitors of different radii. We assumed values typical of SN Ia models, namely  $E_{51} = 1$ ,  $M_c = 1$ ,  $\kappa_{0.2} = 1$ ,  $f_p = 1$ . The emission spectrum was taken to be a blackbody with temperature  $T$  and luminosity  $L$ . The day 0.45  $g$ -band observation of SN 2011fe indicates  $L \sim 10^{40} \text{ erg s}^{-1}$ , which constrains the progenitor radius to  $R \leq 10^{10}$  cm.

Because the impact with a companion star only shocks a portion of the SN ejecta (that within a conical region with opening angle  $\sim 40^\circ$ ), the shock luminosity from the interaction is anisotropic, and will be most prominent for viewing angles nearly aligned with the symmetry axis. Such an orientation occurs  $\sim 10\%$  of the time. Numerical multi-dimensional radiation transport calculations of the dependence of the luminosity on viewing angle<sup>46</sup> show that the luminosity observed  $90^\circ$  ( $180^\circ$ ) from the symmetry axis is about a factor 10 (100) lower than that viewed on-axis. For a red-giant companion ( $a \approx 10^{13}$  cm), the predicted shock luminosity is  $\geq 10^{41} \text{ erg s}^{-1}$  for all viewing angles, ruling out this progenitor system. A  $1 M_\odot$  main-sequence companion ( $a \approx 10^{11}$  cm) has  $L \approx 10^{41} \text{ erg s}^{-1}$  when viewed on-axis, and thus would be consistent with the data if the observer were oriented  $\geq 90^\circ$  from the symmetry axis.

## References

28. Miller, J. S. & Stone, R. P. S. (1993). Lick Obs. Tech. Rep. 66. Lick Obs., Santa Cruz.
29. Filippenko, A. V. The importance of atmospheric differential refraction in spectrophotometry. *PASP* **94**, 715–721 (1982).
30. Horne, K. An optimal extraction algorithm for ccd spectroscopy. *PASP* **98**, 609–617 (1986).
31. Wade, R. A. & Horne, K. The radial velocity curve and peculiar tio distribution of the red secondary star in z chamaeleontis. *ApJ* **324**, 411–430 (1988).
32. Matheson, T., Filippenko, A. V., Ho, L. C., Barth, A. J. & Leonard, D. C. Detailed analysis of early to late-time spectra of supernova 1993j. *AJ* **120**, 1499–1515 (2000).
33. Vogt, S. S. *et al.* HIRES: the high-resolution echelle spectrometer on the Keck 10-m Telescope. In D. L. Crawford & E. R. Craine (ed.) *Society of Photo-Optical Instrumentation Engineers (SPIE) Conference Series*, vol. 2198 of *Society of Photo-Optical Instrumentation Engineers (SPIE) Conference Series*, 362–372 (1994).
34. de Vaucouleurs, G. *et al.* *Third Reference Catalogue of Bright Galaxies. Volume I: Explanations and references. Volume II: Data for galaxies between 0<sup>h</sup> and 12<sup>h</sup>. Volume III: Data for galaxies between 12<sup>h</sup> and 24<sup>h</sup>.* (1991).
35. Munari, U. & Zwitter, T. Equivalent width of NA I and K I lines and reddening. *A&A* **318**, 269–274 (1997).
36. Gehrels, N. *et al.* The Swift Gamma-Ray Burst Mission. *ApJ* **611**, 1005–1020 (2004).
37. Roming, P. W. A. *et al.* The Swift Ultra-Violet/Optical Telescope. *Space Sci. Rev.* **120**, 95–142 (2005).
38. Brown, P. J. *et al.* Ultraviolet Light Curves of Supernovae with the Swift Ultraviolet/Optical Telescope. *AJ* **137**, 4517–4525 (2009).
39. Poole, T. S. *et al.* Photometric calibration of the Swift ultraviolet/optical telescope. *MNRAS* **383**, 627–645 (2008).
40. Oke, J. B. & Gunn, J. E. Secondary standard stars for absolute spectrophotometry. *ApJ* **266**, 713–717 (1983).
41. Thomas, R. C., Nugent, P. E. & Meza, J. C. SYNAPPS: Data-Driven Analysis for Supernova Spectroscopy. *PASP* **123**, 237–248 (2011).
42. Arnett, W. D. Type I supernovae. I - Analytic solutions for the early part of the light curve. *ApJ* **253**, 785–797 (1982).
43. Chevalier, R. A. Early expansion and luminosity evolution of supernovae. *ApJ* **394**, 599–602 (1992).
44. Chevalier, R. A. & Fransson, C. Shock Breakout Emission from a Type Ib/c Supernova: XRT 080109/SN 2008D. *ApJ* **683**, L135–L138 (2008).
45. Piro, A. L., Chang, P. & Weinberg, N. N. Shock Breakout from Type Ia Supernova. *ApJ* **708**, 598–604 (2010).
46. Kasen, D. Seeing the Collision of a Supernova with Its Companion Star. *ApJ* **708**, 1025–1031 (2010).
47. Nakar, E. & Sari, R. Relativistic shock breakouts - a variety of gamma-ray flares: from low luminosity gamma-ray bursts to type Ia supernovae. *ArXiv e-prints* (2011). 1106.2556.
48. Rabinak, I. & Waxman, E. The Early UV/Optical Emission from Core-collapse Supernovae. *ApJ* **728**, 63–71 (2011).
49. Rabinak, I., Livne, E. & Waxman, E. Early emission from type Ia supernovae. *ArXiv e-prints* (2011). 1108.5548.